

Development of a comprehensive PMT optical model for the JUNO experiment

Y. Ren^{a,b} X. Yang^a Y. Wang^c Z. Deng^{a,1} Z. Qin^a A. Olshevskiy^d W. Wang^{e,f} N. Anfimov^d Z. Wang^a G. Cao^{a,b,2}

^a*Institute of High Energy Physics, Chinese Academy of Sciences, Beijing 100049, China*

^b*University of Chinese Academy of Sciences, Beijing 100049, China*

^c*Shandong University, Jinan 250100, China*

^d*Joint Institute for Nuclear Research, Dubna, Moscow Region 141980, Russia*

^e*Sino-French Institute of Nuclear Engineering and Technology, Sun Yat-sen University, Zhuhai 519082, China*

^f*School of Physics, Sun Yat-sen University, Guangzhou 510275, China*

ABSTRACT: There are 17,612 20-inch photomultiplier tubes (PMTs) installed at the Jiangmen Underground Neutrino Observatory (JUNO). Developing a precise optical model for the PMTs is crucial for enhancing the accuracy of detector simulations and refining the energy response model at JUNO. In this study, we established a comprehensive PMT optical model based on prior studies, taking into account the non-uniformity of photon detection efficiency (PDE) across the PMT surface and the variances in PDE as well as reflections among different PMTs. By collecting reflectance data from 669 PMTs and utilizing PDE data from mass testing systems, we estimated the thickness maps of the photocathode (PC) and the anti-reflective coating (ARC) for each PMT. We also determined the collection efficiency (CE) by decomposing PDE with consideration of the optical processes occurring within the PMTs. The refractive index and extinction coefficient of both the PC and ARC, along with the escape factor, were evaluated over a broad wavelength range of 300 nm to 700 nm, covering the entire spectrum of interest for JUNO. Compared to the prediction from a simplified PMT optical model, which assumes uniform PC and ARC across all PMTs of the same type, the further developed PMT optical model yields much more reflectance for HPK PMTs and less for NNVT PMTs, and the change in PDE is at the level of a few percent. This comprehensive PMT optical model also provides a valuable reference for other PMT-based applications.

KEYWORDS: Only keywords from JINST's keywords list please

ARXIV EPRINT: [1234.56789](https://arxiv.org/abs/2601.19081)

¹dengzy@ihep.ac.cn, corresponding author.

²caogf@ihep.ac.cn, corresponding author.

Contents

1	Introduction	1
2	A comprehensive PMT optical model	3
2.1	Recap of the PMT optical model	3
2.2	Extension of the PMT optical model	3
3	PDE and reflectance data	5
3.1	PDE data	5
3.2	Reflectance data	6
4	Results	9
4.1	Thickness map of the PC and ARC	9
4.2	CE	10
4.3	Spectral response of optical properties	11
4.4	Comparison of the average reflection and PDE	12
5	Conclusion	14

1 Introduction

The photomultiplier tube (PMT) has served as an optimal photosensor for numerous neutrino projects over the past few decades and remains pivotal in current and future initiatives. One such project is the Jiangmen Underground Neutrino Observatory (JUNO), which has deployed 17,612 20-inch PMTs and 25,600 3-inch PMTs in its central detector. The spherical arrangement of these PMTs achieves up to 75% photocathode (PC) coverage. Among the 20-inch PMTs, about 5,000 are dynode PMTs manufactured by Hamamatsu Photonics K.K. (HPK), while the remainder are MCP-PMTs produced by Northern Night Vision Technology Co. (NNVT) [1]. These PMTs are used to capture light from the 20 kton liquid scintillator contained within an acrylic sphere with a diameter of 35.4 m. The detailed design of the JUNO detector is described in [2]. JUNO’s primary goal is to determine the neutrino mass ordering and precisely measure the neutrino oscillation parameters by analyzing oscillation patterns within the neutrino energy spectrum from the Taishan and Yangjiang nuclear power plants, located approximately 53 km from the JUNO site. Additionally, JUNO has an extensive physics program focused on detecting neutrinos from various natural sources, as outlined in [3, 4].

A precise understanding of the detector response is crucial for determining the neutrino mass ordering and conducting other physics analyses in JUNO [5]. Specifically, the detector response primarily involves the energy resolution, energy non-uniformity, and energy non-linearity within the JUNO detector. The responses of the PMTs, particularly the photon detection efficiency (PDE),

significantly influence these energy responses and must be carefully managed. Understanding the PDE of PMTs is complex, as it depends on various factors, including the working media, the angle of incidence (AOI) of photons, photon energy, positions where the light hits the PC, and the shape as well as the internal structure of PMTs. The influence of these factors on the PDE is discussed in detail in [6]. Within the JUNO experiment, the PDE of 20-inch PMTs has been thoroughly characterized via the PMT mass testing system, including the average PDE measured by the container system for all PMTs and the PDE uniformity measured by the scanning station system for a subset, with results summarized in [7]. However, the measured PDE cannot be directly used in detector simulations to predict energy responses because the PMTs operate in water within the JUNO detector, rather than in air, and the AOIs, energies, and positions of photons hitting the PMTs differ from those in the mass testing system. In fact, these factors can vary significantly from event to event in the JUNO detector and lead to different PDE. Therefore, a PMT optical model is essential to accommodate all these factors while adhering to constraints from the mass testing data.

A new optical model for PMTs has been proposed in [6], which accounts for the PMT window as a composite structure comprising the glass substrate, a thin anti-reflective coating (ARC), and a PC. The key parameters of this model were determined from detailed measurements performed on three 20-inch PMTs: two from NNVT and one from HPK. By incorporating the optical properties of the PC and ARC obtained from these measurements into the JUNO simulation program, the energy response of the JUNO detector has been evaluated and predicted under the assumption that PMTs of the same type with the identical optical properties of PC and ARC [8]. However, variations in PDE exist among PMTs, and the properties of the PC and ARC could be non-uniform. Moreover, PMT reflectance exhibits significant variation, which must also be taken into account, as light reflected from the PMTs has a substantial impact on the light yield and energy response in the JUNO detector. In this work, these effects are incorporated by extending the PMT optical model originally developed in [6]. The extension utilizes PDE data obtained from both the container system and the scanning station system, as well as reflection data collected in this study. The resulting comprehensive PMT optical model enables the decoupling of quantum efficiency (QE) and collection efficiency (CE) from the measured PDE, while accounting for the non-uniformity of PC and ARC. Specifically, QE is determined based on the photon absorption ratio in the PC and the escape factor, which represents the fraction of photoelectrons that successfully escape from the PC. Using this model, we derived thickness maps of the PC and ARC for all 17,612 20-inch PMTs, along with their corresponding CE values. The model covers the entire range of photon wavelengths relevant to JUNO, from 300 nm to 700 nm. This comprehensive approach also provides valuable insights for other PMT-based projects seeking to improve their detector performance.

The subsequent sections are organized as follows: we first review the PMT optical model developed in [6], followed by a detailed discussion of the comprehensive PMT optical model. We then introduce the PDE data used in this study, and illustrate the method employed for the PMT reflection measurements and report the reflectance results. Subsequently, the extracted basic parameters for the PMT optical simulation are discussed, including the thickness maps of PC and ARC and CE for individual PMTs, as well as the refractive index and extinction coefficient over an extended wavelength range for three types of PMTs. In the end, the comparison of the average reflectance and PDE calculated from the simplified and comprehensive models is presented.

2 A comprehensive PMT optical model

2.1 Recap of the PMT optical model

The PDE could be denoted as a function of the photon wavelength (λ), the AOI (α), and the position (\vec{r}) of the photon hitting the PC of the PMTs. Specifically, the measured PDE can be contributed by multiple positions in addition to the point of incidence on the PC, as a fraction of the incident light could penetrate the PC and propagate within the PMTs. Consequently, the PDE can be expressed as shown in Eq. 2.1 and is discussed in detail in [6]:

$$\text{PDE}(\lambda, \alpha, \vec{r}) = \sum_j a_j(\lambda, \alpha, \vec{r}) \cdot \beta_j \cdot \rho_j(\lambda, \vec{r}) \cdot \text{CE}_j(\vec{r}) = \sum_j a_j(\lambda, \alpha, \vec{r}) \cdot \beta_j \cdot F_j(\lambda, \vec{r}) \quad (2.1)$$

Here, j represents the j -th detected photon, and a_j represents the absorption ratio of the incident light, and ρ_j is the escape factor. The product of ρ and CE is denoted as an F -factor. The coefficient β weights the absorption from different positions that contribute to the measured PDE. In an ideally uniform PC, the positional dependencies of a and ρ would be negligible. While this assumption may hold in certain applications, it is generally not valid for large PMTs, such as those employed in JUNO.

The CE is determined by the electric field within the PMTs, which typically varies with the positions on the PC. By selecting several reference positions with known F -factors on the PC, the F -factor at any other position can be derived through interpolation. Therefore, Eq. 2.1 can be rewritten as:

$$\text{PDE} = \sum_j a_j \sum_{k=1}^n \beta_{jk} F_k \quad (2.2)$$

where β represents the weight coefficient, and F_k denotes the F -factor at the k -th reference point. A procedure for deriving the F -factors at these reference points has been proposed in [6]. The coefficient β can be obtained by simulating the optical processes inside the PMTs using a simulation toolkit. The absorptance a , reflectance, and transmittance of incident photons on the PC can be calculated based on the optical theory, using the known optical properties of the PC and ARC, including the refractive index (n), extinction coefficient (k), and thickness (d). In previous work, reflectivity data collected by immersing PMTs in the linear alkylbenzene are used to extract values for n , k , and d for two NNVT PMTs and one HPK PMT across a wavelength range of 390 nm to 500 nm. These PMTs represent three different types of 20-inch PMTs utilized in the JUNO detector. For NNVT PMTs, there are two types known as NNVT normal-QE PMT and NNVT high-QE PMT, which was produced during the early stages of PMT mass production and manufactured with improved QE achieved through optimized PC technology, respectively.

2.2 Extension of the PMT optical model

The following assumptions have been made to enable the PMT optical model to account for PDE non-uniformity within a single PMT and PDE variations among different PMTs:

- PMTs of the same type share identical spectral responses for the refractive index and extinction coefficient of both the PC and the ARC. The values of n and k obtained in [6], as well as the escape factor ρ , are employed in this study for the three types of PMTs, covering wavelengths

from 390 nm to 500 nm. Utilizing dispersion relations and available data in the literature, we extend this range down to 300 nm and up to 700 nm, encompassing the relevant spectrum for JUNO.

- Variations in QE and reflectance for a single PMT are induced by non-uniform thicknesses of the PC and ARC. The thickness map is determined in this work using Eq. 2.2, with inputs derived from PDE and reflectance data for each 20-inch PMT. These inputs will be discussed in detail in Sec. 3.
- Due to the absence of specific QE information, decoupling the position dependence of QE and CE from the measured PDE exists some problems. Therefore, we assume that the CE remains constant in the PC region for zenith angles smaller than 50 degrees (in regions far from the equator) when calculating the thickness maps of the PC and ARC. Thereafter, the positional dependence of CE and its variations among different PMTs are incorporated into Eq. 2.2.
- For simplification, we assume that both QE and CE are independent of azimuthal angles on the PC. This assumption is a reasonable approximation for the QE of both NNVT PMTs and HPK PMTs, as demonstrated in [7]. Regarding CE, while it is azimuthal angle-dependent for HPK PMTs near the equator due to the orientation of the focusing electrode, the random arrangement of these electrodes during PMT installation in the JUNO detector largely mitigates their impact on energy responses, as contributions from multiple PMTs during physical events sufficiently average out these variations.

Given the assumptions above, the thickness map of the PC and ARC, along with the CE at small zenith angles, can be derived by simultaneously fitting the PDE and reflectance data using Eq. 4.1 for all 20-inch PMTs. To model the position dependence of the thickness for both the PC and the ARC, an empirical formula is employed:

$$d_{PC,ARC} = c_2 \times \theta^2 + c_1 \times \theta + c_0 \quad (2.3)$$

where θ represents the zenith angle of the position on the PC, while c_0 , c_1 , and c_2 are free parameters determined through the fitting process. Fig. 1 illustrates the contours of reflectance (top) and absorptance (bottom) at 415 nm and 420 nm, respectively, calculated as a function of the thicknesses of the ARC (x-axis) and PC (y-axis) for the HPK PMT (left), NNVT normal-QE PMT (middle), and NNVT high-QE PMT (right). The refractive index and extinction coefficient of the ARC and PC reported in [6] are used in these calculations. Notably, the different types of PMTs exhibit distinct dependencies in their thickness maps. The fitting procedure aims to identify the optimal path on the contours that aligns closely with both the reflection and absorption data, the latter of which is inherently incorporated into the PDE data. Once the thickness maps of the PC and ARC are established, absorption ratios can be calculated for any position on the PC. The weight coefficients are obtained by simulating the optical processes within the PMTs using a simulation program developed based on Geant4. Subsequently, the CE at the reference points can be determined using the known PDE values at those points via Eq. 2.2. As a result, a complete CE curve can be constructed for each PMT.

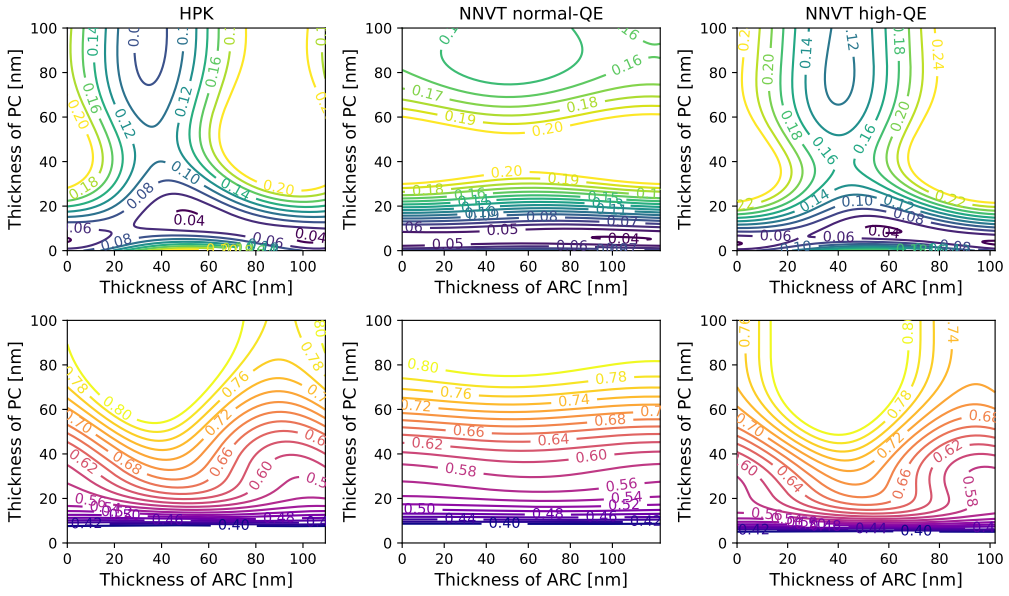


Figure 1: Contours of reflectance (top) and absorptance (bottom) at 415 nm and 420 nm, respectively, as a function of thicknesses of the ARC (x-axis) and PC (y-axis) for the HPK PMT (left), NNVT normal-QE PMT (middle) and NNVT high-QE PMT (right).

3 PDE and reflectance data

In this work, both the PDE results measured by the mass testing systems including the container system and the scanning station system and the newly collected reflectance data are utilized to constrain the thicknesses of the PC and ARC.

3.1 PDE data

For each 20-inch PMT, the PDE is measured using a container system that employs a 420 nm light source to illuminate the entire PMT PC in air. Additionally, a subset of PMTs is evaluated for the PDE uniformity test using a scanning station system, which scans the PC with seven LEDs that provide 420 nm light nearly perpendicular to the surface at seven fixed zenith angles, meanwhile the LEDs can be rotated to cover the different azimuth angles. The PDE obtained from the container system is then corrected to align with the PDE as defined by the scanning station system, which averages the PDE values obtained at the positions of the seven LEDs, weighted by their respective surface areas, and Table 1 summarizes the surface area weights along with the zenith angles for each LED for both NNVT and HPK PMTs. In this study, the PDE values averaged over azimuthal angles for seven zenith angles are utilized to extract the thickness maps of the PC and ARC.

However, since only approximately 3,200 PMTs were evaluated using the scanning station system, it is necessary to develop a method to estimate the PDE values at the seven zenith angles for the PMTs that were not tested in this system in order to constrain their non-uniform PC and ARC as well. A straightforward approach to predict these PDE values is to perform random sampling based on the measured data. To account for the potential dependence of PDE on zenith angles,

Table 1: The zenith angles and the PC area weights of the seven LEDs equipped in the scanning station system [7].

	LED1	LED2	LED3	LED4	LED5	LED6	LED7
Zenith angle (NNVT)	14°	30°	42.5°	55°	67°	77.5°	85°
Area weight (NNVT)	4.85%	8.97%	12.58%	17.21%	19.92%	18.04%	18.43%
Zenith angle (HPK)	13°	28°	41°	55°	66°	79°	85°
Area weight (HPK)	4.51%	8.76%	13.49%	17.11%	20.46%	18.65%	17.03%

a seven-dimensional PDE histogram is constructed using data collected with the scanning station system for each type of PMT, which includes 585 HPK PMTs, 1,719 NNVT normal-QE PMTs, and 939 NNVT high-QE PMTs. The random sampling of the PDE is carried out for each PMT using the seven-dimensional PDE histograms. A normalization factor is applied to the seven sampled values during the sampling process to ensure that the average sampled PDE of each PMT aligns with the PDE results obtained from the container system, where the average PDE is calculated by applying the weights presented in Table 1. This method allows the determination of PDE values at the seven reference positions through sampling for all PMTs that were not tested using the scanning station system.

Since the PDE obtained above encompasses contributions from multiple positions on the PC in addition to the incident position, a detailed PMT optical simulation is conducted to correct for these additional contributions. Utilizing the PMT optical simulation software developed in [6], the detailed structure of the seven LED light sources has been newly implemented in the software, reflecting their real locations and orientations. This simulation allows for accurate accounting of the distributions of the AOI and the beam profile of light impinging on the PMT surface. Fig. 2 illustrates the zenith angle distribution contributing to the total absorption at 420 nm for HPK PMTs shown in red, NNVT normal-QE PMTs in green, and NNVT high-QE PMTs in blue. These results are obtained via the optical simulation for seven LED light sources, and the optical properties of the PC and ARC are derived from [6] with an assumption of uniform them. This figure indicates that the total absorption primarily arises from the incident position of the light beams, which is represented by the peak, and the ratio of the contributions from transmitted photons is depicted in the last panel and is used to correct the PDE by excluding these extra contributions based on their weights. It is observed that the two types of NNVT PMTs exhibit the similar distributions due to their same shape and structure, and compared to HPK PMTs, they gains significantly larger contributions from transmitted photons because of the considerably smaller electrodes within them, which reduces the loss of the transmitted light.

3.2 Reflectance data

The reflectance measurements were carried out before assembling the PMT covers, utilizing the setup developed in this work. In the first stage, a total of 565 20-inch PMTs were randomly selected for testing, which included 276 HPK PMTs, 115 NNVT normal-QE PMTs, and 174 NNVT high-QE PMTs. The reflectance was measured at 415 nm across four different zenith angles, including 0°, 28°, 51° and 72°. In the second stage, only the PMTs tested with the scanning station system were

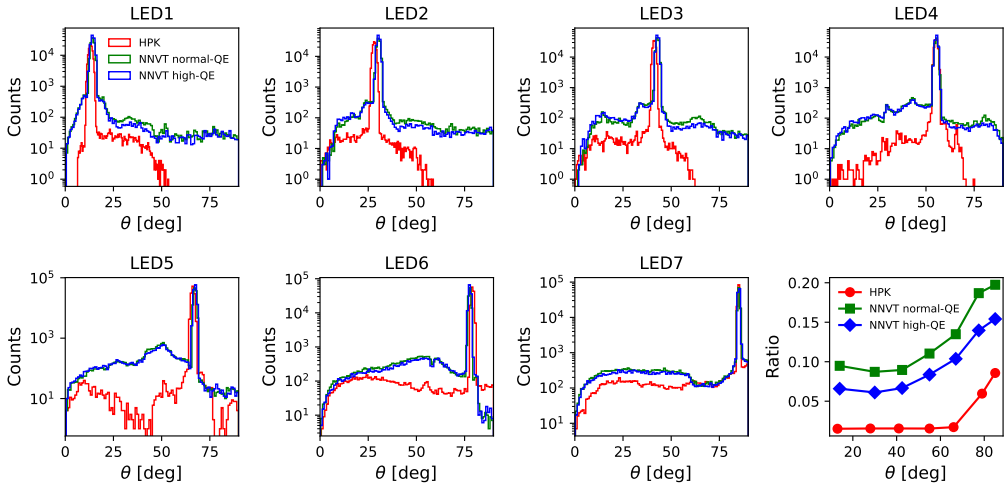


Figure 2: The zenith angle distribution contributing to the total absorption for HPK PMTs shown in red, NNVT normal-QE PMTs in green, and NNVT high-QE PMTs in blue, and the ratio of the contributions from transmitted photons is shown in the last panel.

selected, with measurements taken at four zenith angles and azimuth angle scans with a step of 45° , involving 21 HPK PMTs, 38 NNVT normal-QE PMTs, and 45 NNVT high-QE PMTs.

The schematic diagram of the reflectance measurement setup is shown in Fig. 3. The system consists of an LED light source coupled with an optical fiber, with a central wavelength of 415 nm and a full width at half maximum of 14 nm. An integrating sphere, the ISP-50-8-REFL from Mikropack, is employed to collect the reflected light from the tested samples, along with a spectrometer and a computer for data storage, while a testing mold provides positional information on the PMTs. In the setup, optical fiber #1 transmits light from the LED to the integrating sphere, where the light beam is collimated using a lens integrated at the top of the sphere. The incident light beam exits the sphere at an AOI of 8° through a hole at the bottom, which has a diameter of approximately 8 mm. When a sample is placed over this hole, the reflected light is collected by the integrating sphere, and a fraction of this light is transmitted through optical fiber #2 to the spectrometer, where its intensity is measured as a function of wavelength. By comparing the measured intensity of the test sample with the reference sample of known reflectivity, the reflectance of the test sample can be determined. This measurement does not require dark conditions, as the background spectrum can be directly measured without samples placed over the hole of the integrating sphere. Fig. 4 illustrates an example of the measured spectra: the background (blue), the PMT (green), and the reference sample (orange).

The systematic uncertainty has been carefully estimated, with the relative uncertainty determined to be approximately 2.5%. The primary contributions to this uncertainty arise from the LED stability and the reflectance uncertainty of the reference sample. Additionally, the reflectance of PMT was corrected using the ratio of the reflectance of the flat sample to the curved one for each zenith angle to eliminate the influence of the curvature of the PMT surface on the reflectance. Since no dependence of reflectance on the azimuthal direction was observed, the reflectance values measured at different azimuthal angles are finally averaged for each zenith angle.

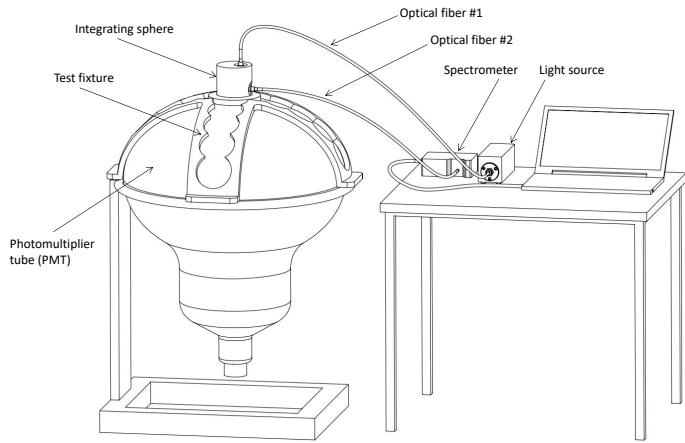


Figure 3: The schematic diagram of the reflectance setup.

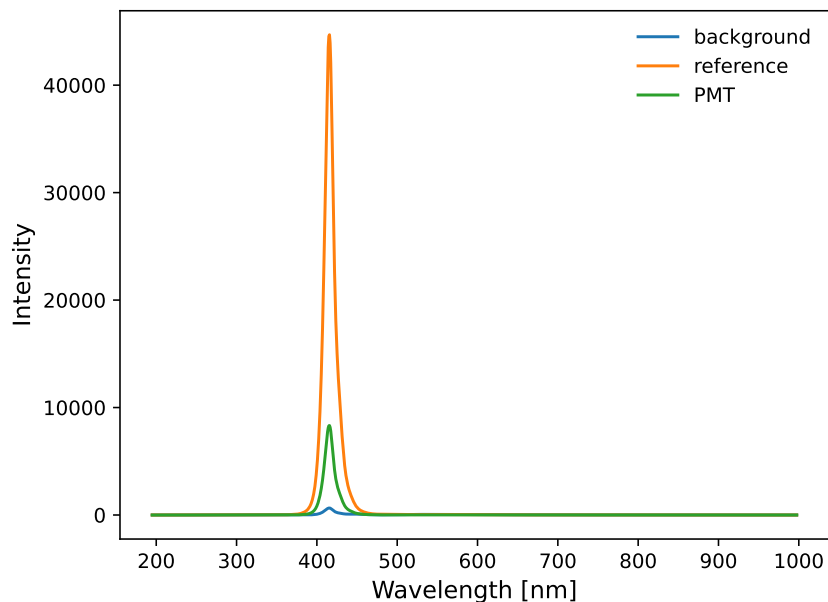


Figure 4: An example of the measured spectra: the background (blue), the PMT (green), and the reference sample (orange).

The measured results are presented in Fig. 5, showing data for all tested HPK PMTs (left), NNVT normal-QE PMTs (middle), and NNVT high-QE PMTs (right), and the solid blue lines represent the average reflectance for each type of PMT. Significant variations in reflectance can be observed across all types of PMTs. Specifically, the average reflectance at the zenith angle of zero degree for HPK PMTs is approximately 5.9%, which is lower than 10.8% and 16.4% observed for the NNVT normal-QE and NNVT high-QE PMTs, respectively. Additionally, the reflectance of HPK PMTs increases in areas closer to the equator; in contrast, the reflectance of NNVT PMTs exhibits a decreasing trend from 0° to about 50°, followed by an increase.

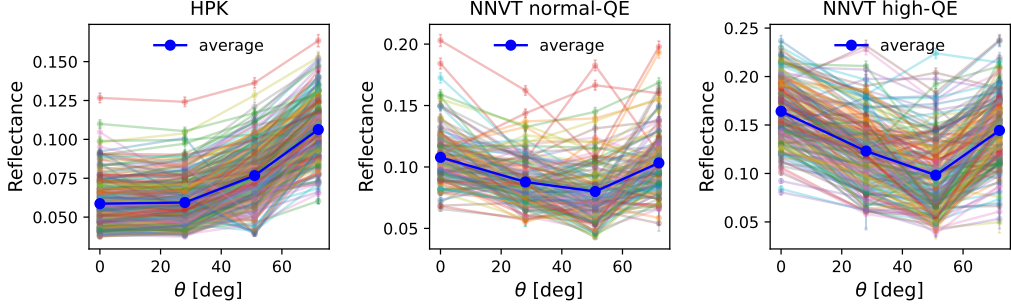


Figure 5: The measured reflectance of the HPK PMTs (left), NNVT normal-QE PMTs (middle), and NNVT high-QE PMTs (right). The solid blue lines shown in the figure represent the average reflectance for each type of PMT.

A similar random sampling approach to that used for estimating PDE is employed to assess the reflectance of PMTs that have not been measured. A four-dimensional reflectance histogram is constructed using the measured data for each type of PMT to account for the positional dependence of reflectance. Since the collected data indicate a weak correlation between reflectance and PDE, this relationship is not considered in the aforementioned sampling process.

4 Results

4.1 Thickness map of the PC and ARC

A chi-squared function is constructed to simultaneously fit the reflectance and PDE data:

$$\chi^2 = \sum_{i=1}^4 \left(\frac{R(\theta_i) - R_{theo}(d_{PC}(\theta_i), d_{ARC}(\theta_i))}{\sigma_R} \right)^2 + \sum_{j=1}^5 \left(\frac{A(\theta_j) - A_{theo}(d_{PC}(\theta_j), d_{ARC}(\theta_j))}{\sigma_A} \right)^2 + \left(\frac{CE - CE_{theo}}{\sigma_{CE}} \right)^2 \quad (4.1)$$

In this equation, $R(\theta_i)$ represents the measured reflectance at the four zenith angles, while R_{theo} and A_{theo} are the calculated reflectance and absorptance, respectively, based on the optical theory.

The predicted CE, CE_{theo} , is set to 0.93 for HPK PMTs and 1.0 for NNVT PMTs. The uncertainties σ_R , σ_A , and σ_{CE} correspond to the measured reflectance, expected absorptance, and expected CE, respectively. Here, σ_{CE} is assumed to be 3%, and σ_A is estimated through error propagation from the measured PDE and its uncertainty, as the absorptance $A(\theta_j)$ can be calculated using:

$$A(\theta_j) = \frac{PDE'(\theta_j)}{\rho \times CE} \quad (4.2)$$

where PDE' represents the corrected PDE, excluding contributions from internal optical processes inside the PMTs. Only the PDE measured at five small zenith angles, namely from LED1 to LED5, are utilized in the fitting process. The value of the escape factor ρ is at 420 nm from [6].

By minimizing Eq. 4.1, the free parameters c_0 , c_1 , and c_2 in Eq. 2.3 can be constrained for both the PC and ARC of each PMT, as well as the temporary CE. An example of the thickness curves derived from the fitting is illustrated in Fig. 6 for the HPK PMT (left), NNVT normal-QE PMT (middle), and NNVT high-QE PMT (right). The thickness of the ARC has been fixed to 49.1 nm for the NNVT normal-QE PMTs, due to its negligible effect on reflectance and absorptance, as demonstrated in Fig. 1. The obtained thickness distributions at the zenith angle of zero are presented in Fig. 7 for all HPK PMTs (left), NNVT normal-QE PMTs (middle), and NNVT high-QE PMTs (right).

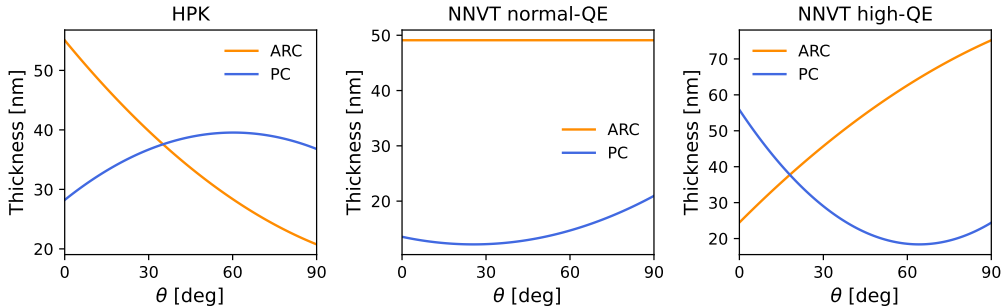


Figure 6: A typical example of the thickness curve of the PC and ARC as a function of the zenith angles for the HPK PMTs (left), NNVT normal-QE PMTs (middle), and NNVT high-QE PMTs (right).

4.2 CE

The aforementioned PMT optical simulation is conducted again for the seven LEDs in the scanning station system by incorporating the obtained thickness map for each PMT into the simulation. This allows us to determine the PDE contributions from various positions on the PC taking into account PC and ARC non-uniformity. From the simulation, both α and β can be derived for the seven reference positions. Using Eq. 2.2, the CE at these reference positions can be calculated for each PMT by solving the system of equations with the known PDE values at each point.

Fig. 8 illustrates the average CE across all PMTs of the same type. It is noted that some CE values are larger than one, which is a consequence of the assumption that the escape factor spectra remains unchanged for each type of PMT since decoupling CE from the escape factor based on the limited data exits challenges in this work.

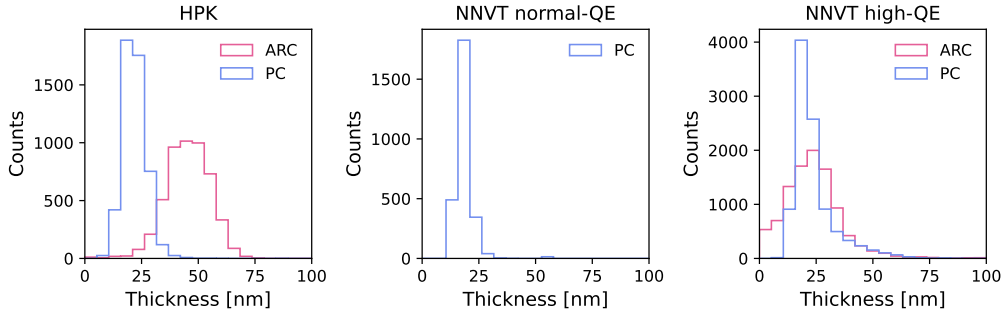


Figure 7: Thickness distributions of the PC and ARC at the zenith angle of zero degree for all HPK PMTs (left), NNVT normal-QE PMTs (middle), and NNVT high-QE PMTs (right).

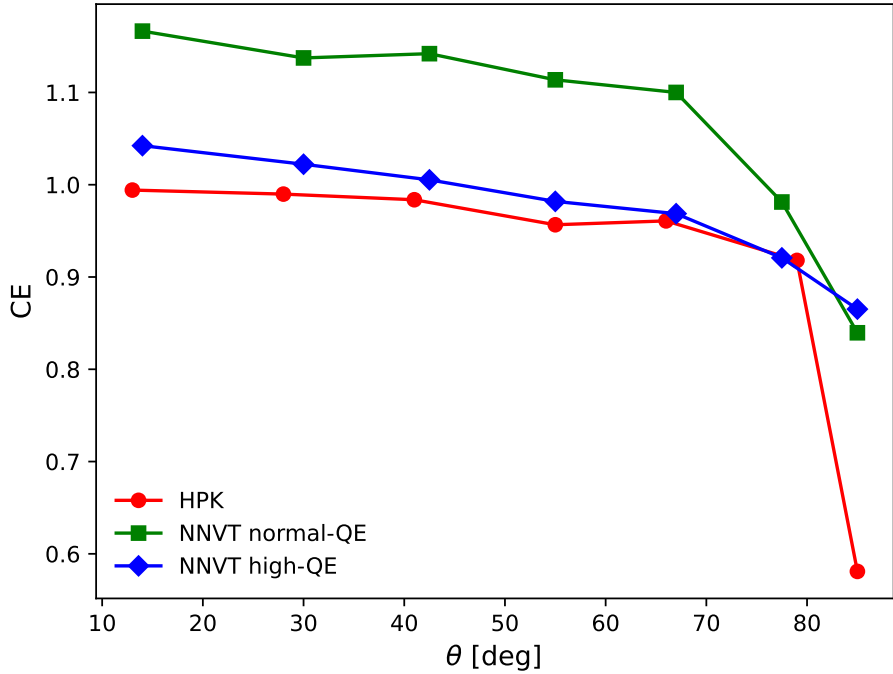


Figure 8: The average CE as a function of the zenith angle for the HPK PMTs (red), NNVT normal-QE PMTs (green), and NNVT high-QE PMTs (blue).

4.3 Spectral response of optical properties

The refractive index and extinction coefficient was measured for the PC and ARC of each type of PMT in [6] within the wavelength range of 390 nm to 500 nm. In this study, the dispersion relation is utilized to extend the refractive index of the ARC, covering the wavelength range of interest for JUNO from 300 nm to 700 nm:

$$n^2 - 1 = \frac{p_0 \lambda^2}{\lambda^2 - p_1} \quad (4.3)$$

where p_0 and p_1 are determined by fitting the measured n values of the ARC between 390 nm and 500 nm. The results for the three types of PMTs are shown in Fig. 9a.

For the PC, n and k values in the wavelength ranges of 300 nm to 390 nm and 500 nm to 700 nm are calculated using the permittivity results for the bialkali PC reported in [9] with the following formula:

$$\epsilon = \epsilon' + i\epsilon'' = n^2 - k^2 + i2nk \quad (4.4)$$

The calculated values in these two ranges are then normalized to the measured values at 390 nm and 500 nm as found in [6]. Fig. 9b illustrates the results for n (solid lines) and k (dashed lines) across the full wavelength range for the HPK PMT (red), NNVT normal-QE PMT (green), and NNVT high-QE PMT (blue).

The escape factor in the ranges of 300 nm to 390 nm and 500 nm to 700 nm is computed based on the measured quantum efficiency spectra in [8] and the respective absorption spectra, which is calculated using the n , k and thickness values for both the PC and ARC in [6], and then the escape factors are normalized to align with the measured curve reported in [6]. The results for the escape factor are shown in Fig. 9c for the three types of PMTs.

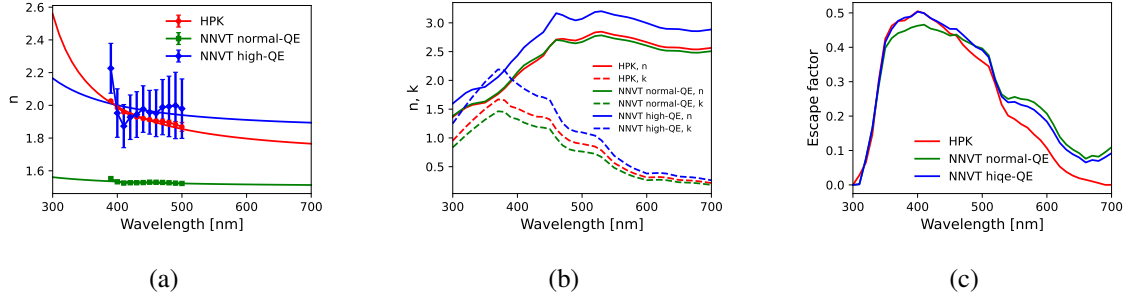


Figure 9: (a) The refractive index of ARC as a function of wavelength for the HPK PMT (red), NNVT normal-QE PMT (green), and NNVT high-QE PMT (blue). (b) The n (solid lines) and k (dashed lines) of the PC as a function of wavelength for the HPK PMTs (red), NNVT normal-QE PMTs (green), and NNVT high-QE PMTs (blue). (c) The escape factor as a function of wavelength for the HPK PMT (red), NNVT normal-QE PMT (green), and NNVT high-QE PMT (blue).

4.4 Comparison of the average reflection and PDE

To evaluate the potential impacts of the comprehensive PMT optical model on the JUNO detector's energy response, we compare the average reflectance and PDE derived from the comprehensive model to those obtained using the simplified PMT optical model, where all PMTs of the same type are assumed to share identical optical properties for the PC and ARC as described in [6].

Figure 10 illustrates the comparison results for the average reflectance (top) and PDE (bottom) at a zenith angle of zero degrees and a wavelength of 420 nm in water, as a function of the AOI, for the HPK PMT (left), NNVT normal-QE PMT (middle), and NNVT high-QE PMT (right). The blue solid lines represent the results with non-uniform PC and ARC, while the orange dashed lines correspond to the simplified model. The green solid lines in the lower panels show the ratio of the two models. Notably, the comprehensive model predicts an increase in reflections for the HPK

PMTs, but a decrease of approximately 30% and 40% in the average reflectance for the NNVT normal-QE and NNVT high-QE PMTs, respectively. The comprehensive model has less than a 2% effect on the average PDE in regions of small AOI for all three PMT types, but a 5% to 10% impact on PDE at large AOI. It is important to note that the PDE values presented here do not include contributions from transmitted photons, which are event-dependent and can be accounted for through simulation.

This comprehensive PMT optical model will be integrated into the JUNO simulation program in the near future, and a more detailed analysis of its effects on energy responses will also be conducted. In addition, the outcomes derived from the comprehensive model will be compared with experimental JUNO data, and the model parameters may be further refined to improve alignment with the actual data.

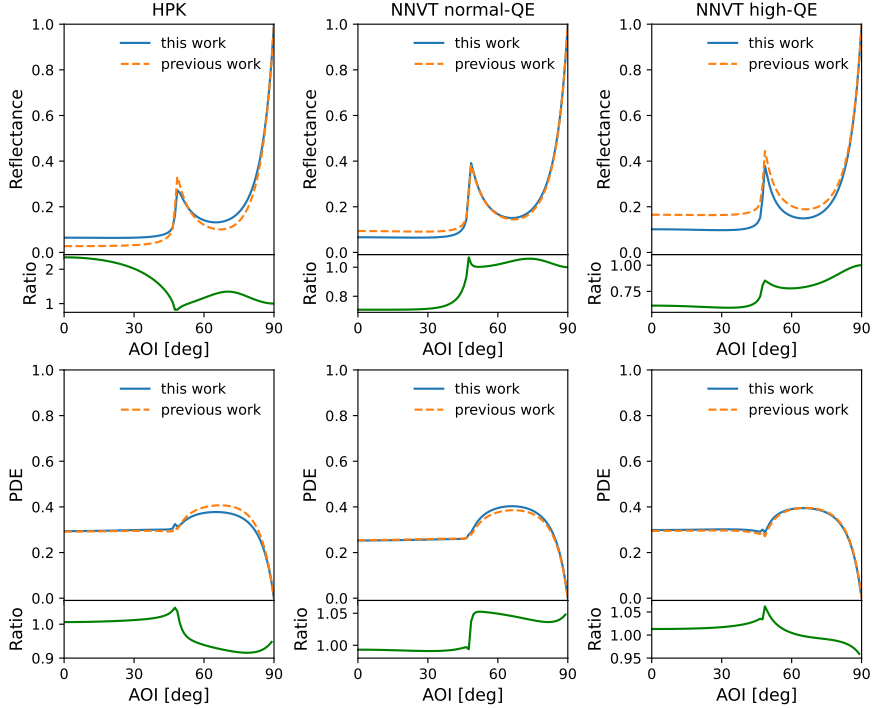


Figure 10: The average reflectance (top) and PDE without the contributions from transmitted photons (bottom) as a function of the AOI for the HPK PMT (left), NNVT normal-QE PMT (middle) and NNVT high-QE PMT (right). The blue solid lines represent the results from the non-uniform ARC and PC, while the orange dashed lines indicate the results from the uniform ARC and PC, and the green solid lines show their ratio.

5 Conclusion

A precise PMT optical model is essential for improving the accuracy of the energy response of the JUNO detector, thereby enhancing the sensitivity and precision of JUNO’s physics outputs. In this work, we developed a comprehensive PMT optical model based on previous research, aiming at extracting some basic optical parameters of PMTs and then precisely simulating the non-uniformity of PDE across the PMT surface and variations in PDE among different PMTs. Reflectance data were collected for 669 PMTs, which were utilized to constrain the thickness map of the PC and ARC for three types of 20-inch PMTs used in JUNO: HPK PMTs, NNVT normal-QE PMTs, and NNVT high-QE PMTs, along with PDE data gathered from both the scanning station system and the container systems used for PMT mass testing.

By performing a joint fit of both the reflectance and PDE data, we obtained the thickness map of the PC and ARC for each PMT. Taking into account the optical processes within the PMTs by simulation, the CE was determined as a function of zenith angle. The refractive index and extinction coefficient of the PC and ARC, as well as the escape factor, was estimated over an extended wavelength range from 300 nm to 700 nm, covering the entire range of interest for JUNO.

Using the new parameters for each PMT, we calculated the average reflectance and PDE, and compared these results with those from the simplified PMT optical model. The results show that the PDE undergoes changes at the level of a few percent, and the reflectance exhibits significant changes of more than 30%. The comprehensive model will be incorporated into the JUNO simulation program, and its effects on the detector’s energy response will also be thoroughly evaluated. Furthermore, additional refinements to the model are anticipated once real JUNO data become available for comparison.

Acknowledgments

We gratefully acknowledge support from the National Natural Science Foundation of China (NSFC) under grant No. 12375196.

References

- [1] Y. Wang, S. Qian, T. Zhao, J. Tian, H. Li, J. Cao et al., *A new design of large area mcp-pmt for the next generation neutrino experiment*, *Nuclear Instruments and Methods in Physics Research Section A: Accelerators, Spectrometers, Detectors and Associated Equipment* **695** (2012) 113.
- [2] JUNO collaboration, *JUNO Conceptual Design Report*, [1508.07166](#).
- [3] JUNO collaboration, *Neutrino Physics with JUNO*, *J. Phys. G* **43** (2016) 030401 [[1507.05613](#)].
- [4] JUNO collaboration, *JUNO physics and detector*, *Prog. Part. Nucl. Phys.* **123** (2022) 103927.
- [5] JUNO collaboration, *Potential to identify neutrino mass ordering with reactor antineutrinos at JUNO*, *Chin. Phys. C* **49** (2025) 033104 [[2405.18008](#)].
- [6] Y. Wang, G. Cao, L. Wen and Y. Wang, *A new optical model for photomultiplier tubes*, *Eur. Phys. J. C* **82** (2022) 329 [[2204.02703](#)].
- [7] JUNO collaboration, *Mass testing and characterization of 20-inch PMTs for JUNO*, *Eur. Phys. J. C* **82** (2022) 1168 [[2205.08629](#)].

- [8] JUNO collaboration, *Prediction of Energy Resolution in the JUNO Experiment*, *Chin. Phys. C* **49** (2025) 013003 [[2405.17860](https://arxiv.org/abs/2405.17860)].
- [9] S. Harmer, R. Downey, Y. Wang and P. Townsend, *Variation in optical constants between photocathodes*, *Nuclear Instruments and Methods in Physics Research Section A: Accelerators, Spectrometers, Detectors and Associated Equipment* **564** (2006) 439.